View Article Online
View Journal

PCCP

Accepted Manuscript

This article can be cited before page numbers have been issued, to do this please use: M. Yang, Y. Zeng, Z. Li, D. Kim, C. Jiang, J. van de Lagemaat and K. Zhu, *Phys. Chem. Chem. Phys.*, 2017, DOI: 10.1039/C6CP08770A.

This is an Accepted Manuscript, which has been through the Royal Society of Chemistry peer review process and has been accepted for publication.

Accepted Manuscripts are published online shortly after acceptance, before technical editing, formatting and proof reading. Using this free service, authors can make their results available to the community, in citable form, before we publish the edited article. We will replace this Accepted Manuscript with the edited and formatted Advance Article as soon as it is available.

You can find more information about Accepted Manuscripts in the author guidelines.

Please note that technical editing may introduce minor changes to the text and/or graphics, which may alter content. The journal's standard Terms & Conditions and the ethical guidelines, outlined in our author and reviewer resource centre, still apply. In no event shall the Royal Society of Chemistry be held responsible for any errors or omissions in this Accepted Manuscript or any consequences arising from the use of any information it contains.

ROYAL SOCIETY OF CHEMISTRY

rsc.li/pccp

Pursuant to the DOE Public Access Plan, this document represents the authors' peer-reviewed, accepted manuscript.
The published version of the article is available from the relevant publisher.

View Article Online
DOI: 10.1039/C6CP08770A

Published on 13 January 2017. Downloaded by National Renewable Energy Laboratory on 17/01/2017 08:41:44.

Do Grain Boundaries Dominate Non-Radiative Recombination in $CH_3NH_3PbI_3$ Perovskite Thin Films?

Mengjin Yang,[a] Yining Zeng,[b*] Zhen Li,[a] Dong Hoe Kim,[a] Chun-Sheng Jiang,[c] Jao van de Lagemaat,[a*] and Kai Zhu[a*]

[a] Chemistry and Nanoscience Center, National Renewable Energy Laboratory, 15013 Denver West Parkway, Golden, CO 80401 (USA)

[b] Biosciences Center, National Renewable Energy Laboratory, 15013 Denver West Parkway, Golden, CO 80401 (USA)

[c] Material Science Center, National Renewable Energy Laboratory, 15013 Denver West Parkway, Golden, CO 80401 (USA)

[*]Corresponding authors: Yining.Zeng@nrel.gov (YZ); Jao.vandeLagemaat@nrel.gov (JvdL); Kai.Zhu@nrel.gov (KZ)

Abstract

Here, we examine GBs with respect to non-GB regions (grain surfaces (GSs) and grain interiors (GIs)) in high-quality micrometer-sized perovskite $CH_3NH_3PbI_3$ (or $MAPbI_3$) thin films using high-resolution confocal fluorescence-lifetime imaging microscopy in conjunction with kinetic modeling of charge-transport and recombination processes. We show that, contrary to previous studies, GBs in our perovskite $MAPbI_3$ thin films do not lead to increased recombination but that recombination in these films happens primarily in the non-GB regions (i.e., GSs or GIs). We also find that GBs in these films are not transparent to photogenerated carriers, which is likely associated with a potential barrier at GBs. Even though GBs generally display lower luminescence intensities than GSs/GIs, the lifetimes at GBs are no worse than those at GSs/GIs, further suggesting that GBs do not dominate non-radiative recombination in $MAPbI_3$ thin films.

Physical Chemistry Chemical Physics Accepted Manuscript

Pursuant to the DOE Public Access Plan, this document represents the authors' peer-reviewed, accepted manuscript.
The published version of the article is available from the relevant publisher.

View Article Online
DOI: 10.1039/C6CP08770A

Published on 13 January 2017. Downloaded by National Renewable Energy Laboratory on 17/01/2017 08:41:44.

Physical Chemistry Chemical Physics Accepted Manuscript

Introduction

During the past several years, the world has witnessed rapid development of a new solar cell technology based on lead halide perovskites (e.g., $CH_3NH_3PbI_3$ or $MAPbI_3$).[1-8] Advancements in material synthesis, device fabrication and modeling, and fundamental structural/photophysical properties have been summarized in several recent reviews.[9-11] Several groups have demonstrated perovskite solar cells (PSCs) of about 20% power conversion efficiency. A key factor to this unprecedented success is the development of solution chemistry and engineering approaches for controlling the morphology and composition of hybrid perovskites. Recent efforts have centered on increasing grain size while maintaining compact film morphology.[12-16] We found that using a non-stoichiometric precursor with slight (~20%) excess of MAI can compensate for the rapid loss of MAI (and delays the formation of the PbI_2 phase) during annealing, facilitating the growth of $MAPbI_3$ with larger, more-textured micrometer-sized grains.[17] Interestingly, a higher device performance is often observed with larger grain size in these studies, which has led to the common belief that grain boundaries (GBs) in polycrystalline perovskite thin films dominate non-radiative recombination (NRR) over the non-GB regions (including both grain surfaces (GSs) and grain interiors (GIs)) and thus should be minimized.[18] Consistent with this notion, a recent study using confocal fluorescence microscopy found that the photoluminescence (PL) intensity at a GB was weaker than that in the GS/GI, and attributed this weaker PL to a higher degree of NRR at GBs.[19] However, the carrier diffusion away from the confocal spot—which affects the PL decay kinetics and intensity—was not considered in this early PL imaging study. Similarly, other studies also attributed the lower PL intensity to faster recombination associated with additional NRR channels,[20, 21] although in these studies the difference between the GB and non-GB regions was not resolved. Recently, certain molecular treatments (e.g., guanidinium and pyridine) were shown to be effective for improving carrier lifetime and device performance, and this improvement was often attributed to the potential passivation of defects at GBs.[13, 19, 22] However, such treatments also affect the grain surface and film morphology (e.g., larger grain size and reduced pinholes), and could just as well affect the bulk of the grains (e.g., bulk crystallinity and defect density). Thus, the exact role of these treatments with respect to GBs remains unclear. The implications of these studies about perovskite GBs seem to be in contrast with an early first-principles study that suggests that GBs in polycrystalline perovskite are, in general, benign due to the lack of deep-level trap states.[23]

Pursuant to the DOE Public Access Plan, this document represents the authors' peer-reviewed, accepted manuscript.
The published version of the article is available from the relevant publisher.

View Article Online
DOI: 10.1039/C6CP08770A

Published on 13 January 2017. Downloaded by National Renewable Energy Laboratory on 17/01/2017 08:41:44.

However, a recent theoretical study found that while GBs may be major recombination sites in the pure iodide material, they could become passivated.[24]

Noteworthy is that perovskite films prepared without any special treatments have also led to highly efficient (~17%–20%) PSCs by various groups,[17, 25, 26] further implying that GBs may not be dominant NRR centers in polycrystalline perovskites. Moreover, in a clear contrast with the assumption that GBs are problematic, our recent time-resolved microwave conductivity (TRMC) studies of films with varying grain sizes suggests that GBs do not act as recombination centers, but do limit lateral diffusion of carriers.[27] Developing strategies to passivate GBs has been considered as the determining factor for the success of high-efficiency polycrystalline copper indium gallium diselenide (CIGS) and CdTe thin-film solar cells.[28, 29] It is expected that a timely fundamental understanding of the exact role(s) of GBs with respect to the non-GB regions in polycrystalline perovskite films will be critical to continue the rapid development of PSCs as well as other applications.

Here, we directly probe perovskite GBs with respect to their interiors/surfaces using spatially resolved confocal fluorescence-lifetime imaging microscopy (FLIM) in conjunction with theoretical modeling. Perovskite $MAPbI_3$ thin films were prepared by following our previously published procedures[17] using a non-stoichiometric precursor to ensure that the grain size is sufficiently large for the spatially resolved imaging studies. Analysis of our FLIM results, coupled with modeling and surface-potential mapping, revealed several important observations regarding the roles of GBs and grain sizes on charge transport and recombination in perovskite $MAPbI_3$ thin films. We show that weaker luminescence intensities do not generally correspond to shorter lifetimes and therefore higher recombination, which is frequently assumed in this field. We also find that GBs in these perovskite $MAPbI_3$ films are impervious to photogenerated carriers, which is likely associated with a potential barrier at GBs. In comparison to the non-GB regions, GBs display similar or longer luminescence lifetimes despite lower luminescence intensities, suggesting that GBs do not dominate recombination in these perovskite $MAPbI_3$ films.

Experimental

Physical Chemistry Chemical Physics Accepted Manuscript

Pursuant to the DOE Public Access Plan, this document represents the authors' peer-reviewed, accepted manuscript.
The published version of the article is available from the relevant publisher.

View Article Online
DOI: 10.1039/C6CP08770A

Published on 13 January 2017. Downloaded by National Renewable Energy Laboratory on 17/01/2017 08:41:44.

Sample preparation. Either cover glass or fluorine-doped tin oxide (FTO) was used for substrates. FTO substrate (TEC 15, Hartford Glass Co) was patterned by wet-etching. Pre-patterned FTO was cleaned in a base bath overnight and then deposited with a thin compact TiO_2 layer by spray pyrolysis using 0.2 M titanium diisopropoxide bis(acetylacetonate) in a 1-butanol solution at 450°C. The substrate was further annealed at 450°C for 1 h. The perovskite $MAPbI_3$ films were deposited by using a non-stoichiometric precursor with excess of organic salt as detailed in our previous report.[17] For FLIM measurement, the perovskite film was deposited directly on a cover glass substrate. For solar cells, the perovskite film was deposited on the TiO_2-coated FTO substrate followed by spin-coating a hole transport layer (HTL) at 4,000 rpm for 35 s. HTL solution was made of 80 mg 2,2',7,7'-tetrakis(N,N-dip-methoxyphenylamine)-9,9'-spirobifluorene (Spiro-MeOTAD; Merck), 30 μL bis(trifluoromethane) sulfonimide lithium salt stock solution (500 mg Li-TFSI in 1 mL acetonitrile), 30 μL 4-tert-butylpyridine (TBP), and 1 mL chlorobenzene solvent. Finally, a metal contact was formed by thermal evaporated 150-nm Ag.

Film and device characterization. X-ray diffraction (XRD) of the perovskite thin films was characterized using an X-ray diffractometer (Rigaku D/Max 2200) with Cu Kα radiation. Absorption spectra were measured by a UV/vis spectrometer (Cary-6000i). A Quanta 600 Field emission scanning electron microscope (FESEM) was used to characterize the morphology of the perovskite thin films. The current density–voltage (J–V) characteristics of the cells were carried out using a 2400 SourceMeter (Keithley) under simulated one-sun AM 1.5G illumination (100 mW cm^{-2}) (Oriel Sol3A Class AAA Solar Simulator, Newport Corporation). External quantum efficiency (EQE) was measured using a solar cell quantum efficiency measurement system (QEX10, PV Measurements). To determine the actual power output, stabilized power output was performed by a potentiostat (VersaSTAT MC, Princeton Applied Research) near the maximum power-output point.

FLIM characterization. The FLIM measurement was carried out on a PicoQuant MicroTime 200 FLIM system installed on an Olympus IX71 inverted microscope. A 405-nm laser excitation source (PicoQuant LDH-P-C-405B) was operated at 2.5 MHz. The excitation fluence was about 3 μJ/cm^2 per pulse, which corresponds to an excitation intensity of about 6×10^{17} cm^{-3} at the confocal spot after the initial laser excitation. The laser beam was focused on the sample through

Physical Chemistry Chemical Physics Accepted Manuscript

Pursuant to the DOE Public Access Plan, this document represents the authors' peer-reviewed, accepted manuscript.
The published version of the article is available from the relevant publisher.

View Article Online
DOI: 10.1039/C6CP08770A

Published on 13 January 2017. Downloaded by National Renewable Energy Laboratory on 17/01/2017 08:41:44.

a high numerical-aperture objective lens (Olympus PlanApo 100x/1.45 oil). The sample was mounted on a P733 stage (Physik Instrumente) for raster scanning. The epi-fluorescence emission from the sample was collected through the same objective lens, filtered by a 430-nm long-pass filter (Chroma HQ430LP) and a 50-µm pinhole before detected by a SPAD module (Micro Photon Devices) and processed by a time-correlated single-photon counting (TCSPC) system PicoHarp 300 (PicoQuant). FLIM images were analyzed by PicoQuant SynPhoTime (V5.3.2.2).

KPFM characterization. Based on the noncontact mode of atomic force microscopy (AFM), KPFM measures contact potential difference (CPD) between the AFM probe and a sample by probing the Coulomb force. Because the electrostatic potential of the probe stays constant during scanning, the CPD mapping gives the electrostatic potential of the sample with ~30-nm resolution. During scanning, the workfunction of the probe stays unchanged and the relative scale of the electrostatic potential of the sample is mapped. The AFM platform (Veeco D5000 and Nanoscope V) is set up in an Ar glove box with both O_2 and H_2O concentrations < 0.1 ppm. The first resonant oscillation frequency (50–70 kHz) of the cantilever (Nannosensor, PPP-EFM) was used for the AFM topographic imaging, and the second resonant frequency (300–400 kHz) was used for the KPFM potential imaging, which enhanced the voltage noise level to ~10 mV in atmospheric pressure. The AC voltage used for oscillating the cantilever was 1 V. The Kelvin probe voltage (DC) was generated by a negative feedback analog circuit, using the cantilever oscillation signal as the feedback source. The AC+DC voltage was applied to the probe and the sample was grounded. There is no observable effect of the AFM laser on potential imaging.

Physical Chemistry Chemical Physics Accepted Manuscript

Pursuant to the DOE Public Access Plan, this document represents the authors' peer-reviewed, accepted manuscript.
The published version of the article is available from the relevant publisher.

View Article Online
DOI: 10.1039/C6CP08770A

Published on 13 January 2017. Downloaded by National Renewable Energy Laboratory on 17/01/2017 08:41:44.

Results and Discussion

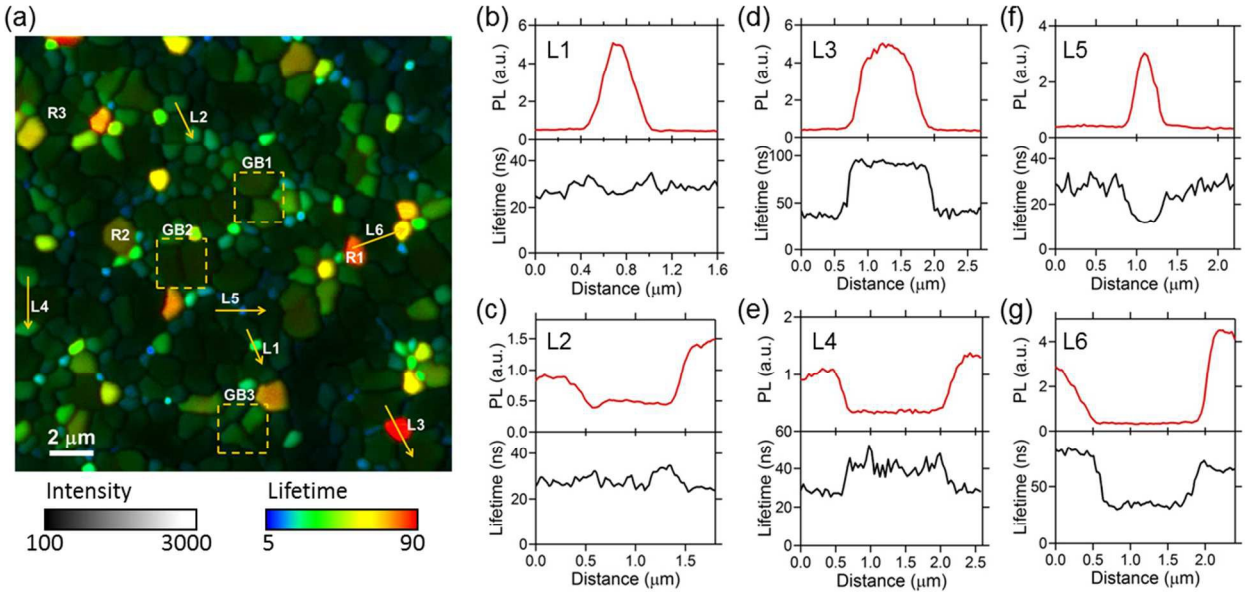

Figure 1. Typical FLIM imaging results. (**a**) FLIM image of a perovskite $MAPbI_3$ thin film deposited on a glass slide. The imaging area is 20×20 μm^2 with 512×512 pixels. Typical FLIM intensity and lifetime line scans across three neighboring grains with different intensity and lifetime characteristics: similar lifetime with (**b**) stronger or (**c**) weaker intensity in the middle grain; longer lifetime with (**d**) stronger or (**e**) weaker intensity in the middle grain; and shorter lifetime with (**f**) stronger or (**g**) weaker intensity in the middle grain. The corresponding line profiles (L1–6) are labeled in the FLIM image with arrows indicating the scan direction.

Figure 1a shows the typical FLIM image of a perovskite $MAPbI_3$ thin film deposited on a glass slide. The different colors correspond to different FLIM lifetimes calculated from the FLIM setup following a fast barycenter average method.[30] The brightness of the image corresponds to the total counts (or intensity) of the luminescence events at each pixel. The respective intensity and lifetime images are shown in Figure S1. The apparent grain sizes and shapes are consistent with the scanning electron microscopy (SEM) image of the perovskite film (Figure S2). Both the ultraviolet-visible (UV-vis) absorption spectrum (Figure S3) and X-ray diffraction pattern (Figure S4) indicate good optical and structural quality of the perovskite thin film used in the FLIM study. Also noteworthy is that planar PSCs using a standard cell configuration (i.e., perovskite sandwiched between a compact TiO_2 layer for electron collection and a hole transport layer based on spiro-MeOTAD) exhibit >18% stabilized efficiency output for layers produced the same way as those studied here (Figure S5). The good structure and device properties further ensure that the FLIM results are not affected by simple structural defects resulting from poor

Physical Chemistry Chemical Physics Accepted Manuscript

Pursuant to the DOE Public Access Plan, this document represents the authors' peer-reviewed, accepted manuscript.
The published version of the article is available from the relevant publisher.

View Article Online
DOI: 10.1039/C6CP08770A

Published on 13 January 2017. Downloaded by National Renewable Energy Laboratory on 17/01/2017 08:41:44.

perovskite processing. Three observations can readily be made by examining this FLIM image. (1) The grain boundaries have weaker (darker) confocal luminescence intensity than the corresponding grains. (2) Each grain has approximately a single homogeneous luminescence lifetime and intensity. (3) There is a wide distribution of both the intensity and lifetime values among grains. These observations suggest that GBs are impervious to charge carriers; otherwise, no contrast in either lifetime or intensity could be observed. This is consistent with the Kelvin probe force microscopy (KPFM) measurement of the potential distribution of the perovskite film. It shows a potential barrier at GBs in our $MAPbI_3$ perovskite films (Figure S6 and Supplementary Note 1); this barrier could hinder carrier transport across the GBs. It is noteworthy that multiple samples were studied over about a 6-month time period. Some representative images are shown in Figure S7 and they are consistent with the image shown in Figure 1a. Moreover, we have verified that the film doesn't degrade during the FLIM measurement (Figure S8). To further illustrate the wide grain-to-grain variations of the luminescence lifetime and intensity, Figures 1b–g show several typical line-scans of FLIM intensity and lifetime profiles across three neighboring grains with different intensity and lifetime characteristics. These line profiles are labeled as L1–6 in the FLIM image with arrows indicating the scan direction. In comparison to the two neighboring grains, the middle grain could have a shorter, similar, or longer lifetime, regardless of their relative luminescence intensities. This does not imply that intensity and lifetime are uncorrelated, just that there is no simple explanation based on previous literature reports. It was noted previously that there could be very small (<2–3 nm) spectral shift among grains,[31] which is insignificant comparing to these observed FLIM variations and has no influence on the measurements presented here.

Because each grain has about uniform luminescence lifetime and intensity and has a clear boundary with weaker (darker) luminescence intensities, we were able to choose each grain as a region of interest to determine the PL lifetime and intensity for each grain. This allowed us to get a statistical analysis of the grain-to-grain variations of the PL lifetime and intensity, which further enabled us to evaluate the correlation between the grain lifetime and intensity, as well as their possible dependence on the grain size.

Physical Chemistry Chemical Physics Accepted Manuscript

Pursuant to the DOE Public Access Plan, this document represents the authors' peer-reviewed, accepted manuscript.
The published version of the article is available from the relevant publisher.

View Article Online
DOI: 10.1039/C6CP08770A

Published on 13 January 2017. Downloaded by National Renewable Energy Laboratory on 17/01/2017 08:41:44.

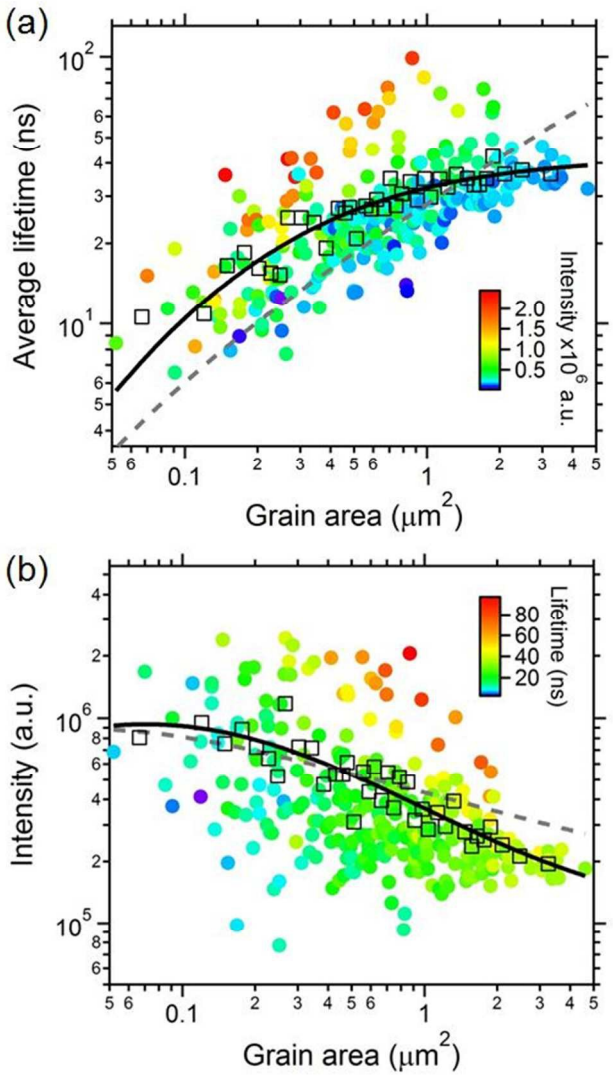

Figure 2. Kinetic modeling of FLIM results. The solid circles represent the calculated (**a**) average grain PL lifetime and (**b**) PL intensity (normalized by grain area) as a function of grain area. The open squares represent the bin-average of grain PL lifetime/intensity with respected to grain sizes. In both (a) and (b), the solid line represents a global fitting to the grain PL lifetime/intensity (solid circles) based on a surface recombination model (i.e., negligible GB recombination), whereas the dashed lines assume that non-radiative recombination at GBs dominates the recombination kinetics. The fits are performed on the full data set instead of the bin-averaged data. The details of these fittings are given in the text. About 300 individual grains from the FLIM image (Figure 1a) were analyzed.

Figures 2a and 2b show, respectively, the calculated average grain PL lifetime (details in Figure S9) and PL intensity (normalized by grain area) as a function of grain area. There were about 300 individual grains from the FLIM image analyzed to generate these plots. The open squares show the same data bin-averaged with respect to grain size for 8 grains. Performing the

Physical Chemistry Chemical Physics Accepted Manuscript

Pursuant to the DOE Public Access Plan, this document represents the authors' peer-reviewed, accepted manuscript.
The published version of the article is available from the relevant publisher.

View Article Online
DOI: 10.1039/C6CP08770A

Published on 13 January 2017. Downloaded by National Renewable Energy Laboratory on 17/01/2017 08:41:44.

same analysis on other samples and images gives the same result. The grain area varies from about 0.05 to 3.6 μm^2, corresponding to an average grain size from about 0.25 to 2.1 μm. Although there is a significant spread in the data points for both PL lifetime and intensity as a function of grain area, a clear overall trend can be observed for both plots: the grain PL lifetime increases with grain area, whereas the grain PL intensity (per area) decreases slightly with grain area. To interpret this apparent trend, it is essential to have a good understanding of the charge-carrier dynamics during the confocal PL decay measurement.

Immediately after excitation, carriers start diffusing away from the initial excitation spot. Assuming an infinitely large grain (i.e. the carriers never reach a GB within the timeframe of the experiment), the confocally detected PL intensity is determined by a function that describes the carrier density inside the confocal spot:

$$I_{PL} = \frac{\sigma_0^2}{2Dt+\sigma_0^2} \exp\left(-\frac{t}{\tau_{PL}}\right), \quad (1)$$

in which σ_0 is the standard deviation of the focused beam profile, which is about 100 nm in our setup (Figure S10), and D is the average diffusion coefficient of both types of carriers. The details of the derivation and discussion of Equation 1 are given in Supplementary Note 2. We find that Equation 1 fits the results well but only for the very largest grains (Figures S11 and S12), yielding an effective carrier diffusion coefficient of 0.095±0.010 cm^{2}s^{-1}. This value means that the average time to diffuse all the way across (and therefore equilibrate) a 1-μm^2 grain is about 8 ns. In the Supplementary Materials, this is further proven by a multiphysics (COMSOL) model considering a full drift/diffusion model for charge carriers that considers surface and grain boundary recombination as well as photon recycling (Figure S13). This fully 3D model shows that photon recycling has no considerable influence on the confocal PL experiment (Figure S14). It also explains that Equation 1 only describes the experimental data for the very largest grains and not for the majority of the grains because the GBs are not transparent to carriers and as soon as the carriers reach the GBs, the grain has equilibrated. This is consistent with the FLIM image in Figure 1a, where it is clear that the confocal PL intensity varies between grains, as does the effective PL lifetime (Figures. 1b–g). Therefore, one can assume that after a few ns, the photogenerated carrier (electron) density n is given by a simple relation that links the initial

Physical Chemistry Chemical Physics Accepted Manuscript

Pursuant to the DOE Public Access Plan, this document represents the authors' peer-reviewed, accepted manuscript.
The published version of the article is available from the relevant publisher.

View Article Online
DOI: 10.1039/C6CP08770A

Published on 13 January 2017. Downloaded by National Renewable Energy Laboratory on 17/01/2017 08:41:44.

concentration in the beam area n_0 to the area of the beam A_b and the area of the grain A_g: as in $n = fn_0$, where f is given by $\frac{d_0}{d}A_b/A_g$, where d_0 is the average film thickness that n_0 is referenced to, and d is the thickness of the grain under study. For initial analysis, we assume that $d = d_0$. An analogous relation applies to the photogenerated hole concentration p. Also, for carrier concentrations homogeneous in the grains after initial diffusion, one can write Equation 2 for the time derivative of the electron concentration taking into account Auger recombination, radiative (band-to-band) recombination, and non-radiative monomolecular recombination, and assuming that $p \approx n$,[32] which is true for moderately high excitation densities where the photogenerated carrier density overwhelms the background as well as saturates any carrier traps and for situations where carrier diffusion to the grain boundaries is much faster than any of the recombination mechanisms:

$$\frac{dn}{dt} = -An^3 - Bn^2 - Cn \tag{2}$$

The non-radiative recombination term C can be described as the sum of bulk (k_{nrb}), top and bottom surface, and grain-boundary recombination

$$C = k_{nrb} + \frac{2A_gR_s}{V} + \frac{A_{gb}R_{gb}}{V} = k_{nrb} + \frac{2R_s}{d} + \frac{2\sqrt{\pi}R_{gb}}{\sqrt{A_g}} \tag{3}$$

in which $A_g$is the top area of the grain, V is its volume, R_s is the surface recombination constant (in cm/s) for top and bottom surfaces, A_{gb} is the area of the grain boundaries, R_{gb} is the surface recombination rate of carriers at the grain boundaries, and d is the grain thickness. The right-hand side of Equation 3 assumes circular grains and that the top and bottom surfaces have equal recombination rates. The equation for different shapes of grains does not differ more than 10% from the expression in Equation 3. It is clear from these equations, that the confocal FLIM measurement cannot separate bulk (k_{nrb}) and surface recombination owing to the rapid equilibration of carriers throughout the thickness of the film (normally a few hundred nanometers); however GB recombination is easily separated from bulk and surface as only GB recombination depends on the grain size. In the rest of this paper, we will neglect the

Physical Chemistry Chemical Physics Accepted Manuscript

Pursuant to the DOE Public Access Plan, this document represents the authors' peer-reviewed, accepted manuscript.
The published version of the article is available from the relevant publisher.

View Article Online
DOI: 10.1039/C6CP08770A

Published on 13 January 2017. Downloaded by National Renewable Energy Laboratory on 17/01/2017 08:41:44.

contribution of bulk monomolecular recombination, but it is important to realize that we cannot distinguish between bulk and surface recombination in this experiment.

To find the apparent quantum yield and lifetime, we can assume that immediately after the initial carrier equilibration throughout the grain, the carrier concentration is given by fn_0. We also assume pseudo-first order behavior for simplicity. The amount of fluorescence detected in the confocal setup can then be derived from Equation 2:

$$I_{PL} = \beta \frac{fBn_0}{Af^2n_0^2 + fBn_0 + C} + O \ . \tag{4}$$

where β is a constant related to the detection efficiency of the microscope and the light out coupling efficiency of the film, and O is an offset that describes scattered or background light being detected in the setup. The fraction $fBn_0/(Af^2n_0^2 + fBn_0 + C)$ can be interpreted as the apparent quantum yield for confocal PL.

We can also derive from Equation 2 the observed pseudo first-order *radiative* lifetime:

$$\frac{\tau^{-1}}{2} = Af^2n_0^2 + Bfn_0 + C \ . \tag{5}$$

Figures 2a and 2b show simultaneous (global) fits of Equations 4 and 5 (with C given by Equation 3) to the experimental results for the situation where both surface and GB recombination can occur (solid lines) and for the situation where only GB recombination occurs (dashed lines). The parameter f varies with grain areas ranging over two orders of magnitude, resulting in two orders of magnitude change in the effective carrier density in the grains. The fits also assume that the trimolecular and bimolecular recombination rates are given by A = 7×10^{-29} cm^6s^{-1} and B = 10^{-10} cm^3s^{-1} in accordance with previous results.[32, 33] The values of rates A and B were held constant because they are well-established intrinsic material properties. It is clear that GB recombination by itself cannot explain the observations accurately. While the fits were performed to the full set of data, it is clear that they very closely follow the bin-averaged data making it even more clear that GB recombination cannot explain the data. By including surface recombination in analysis, we can estimate the surface and grain boundary recombination velocities from the fits to be 152.1 ± 1.2 $cm.s^{-1}$ and 6.8 ± 2.7 $cm.s^{-1}$, indicating that

Pursuant to the DOE Public Access Plan, this document represents the authors' peer-reviewed, accepted manuscript.
The published version of the article is available from the relevant publisher.

Physical Chemistry Chemical Physics Accepted Manuscript

View Article Online
DOI: 10.1039/C6CP08770A

Published on 13 January 2017. Downloaded by National Renewable Energy Laboratory on 17/01/2017 08:41:44.

recombination at the GBs is more than an order of magnitude slower. From these values and Equation 3, it is estimated that the two processes respectively contribute 1.2×10^{7} s^{-1} and 3.4×10^{6} s^{-1} to C for a 0.5 μm^2 grain, less for larger grains. Only for the very smallest grains can the GB contribution be large enough to be of importance but no grains in the studied set have a GB contribution larger than the surface contribution. Secondly, the kinetic model shown above cannot discriminate between carriers recombining at the GBs and carriers crossing the GBs to the neighboring grains so even this small contribution to C might not represent any actual recombination.

The complex dependence of the luminescence intensity and lifetime on grain size seen in Figures 2a and 2b can be explained from this model by realizing that at small grain sizes, the carrier density after equilibration across the grains stays high and carriers are lost to trimolecular recombination, leading to an initial increase in luminescence intensity and a relatively short lifetime because larger grains mean less trimolecular recombination. When further increasing the grain size (or decreasing carrier density due to carriers equilibrating across the grain), Auger recombination becomes negligible and the confocal PL intensity decreases because the effective carrier density decreases and monomolecular recombination starts taking over. At the same time, the PL lifetime levels off because it is no longer shortened by Auger recombination and becomes determined by the non-radiative recombination rate. At some point for very large sizes, the carrier density after equilibration becomes so small that a regime not explicitly considered here will take over where one needs to consider the continuity equations for electrons, holes, and trapped electrons and holes separately. In this case, it is expected that the PL intensity scales with the excitation intensity $n_0^{3/2}$ instead of the linear dependence predicted by Equation 4.[31] At our largest grain size, $fn_0 = 6.5 \times 10^{15}\ cm^{-3}$, which is in a regime where this could be the case. This does however not affect the analysis of the PL lifetime but might affect the data at the very largest grain sizes. A thorough investigation of the dependence of the FLIM intensity as a function of excitation intensity would be required to further investigate this possibility. In our setup is not currently possible to perform this experiment but we are planning modifications to do this.

Physical Chemistry Chemical Physics Accepted Manuscript

Pursuant to the DOE Public Access Plan, this document represents the authors' peer-reviewed, accepted manuscript.
The published version of the article is available from the relevant publisher.

View Article Online
DOI: 10.1039/C6CP08770A

Published on 13 January 2017. Downloaded by National Renewable Energy Laboratory on 17/01/2017 08:41:44.

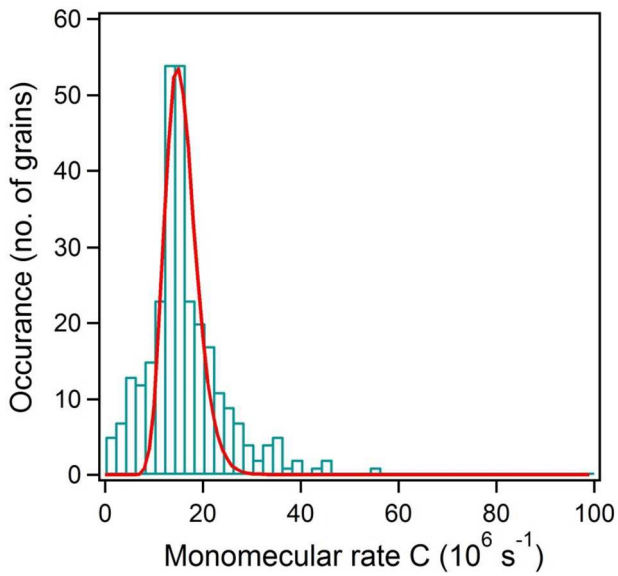

Figure 3. Distribution of the monomolecular recombination rate constant *C*. The distribution of *C* is centered around $C = 1.62\times10^7$ s^{-1}. The continuous line shows the expected distribution if the variation in *C* was due to a variation in the film thickness.

Another way to assess the monomolecular recombination rate is to transform the lifetime data according to Equation 5. Since *A*, *B*, and n_0 are known, we can transform this data to values for *C*, as shown in Figure 3. This shows an almost symmetrical distribution of *C* with an average value of $C = 1.62\times10^7$ s^{-1} in line with previous results for the latter.[32, 33] The variation in *C* is likely due to variations in the surface recombination velocity due to variations in the film thickness (Equation 3). The continuous line in Figure 3 shows that the variation in thickness as seen in the AFM plot (Figure S6) results in a distribution of possible *C* values. Another possible source of spread in *C* is variations in the number of interface traps that each grain has due to simple Poisson statistics and limited area per grain. For an interfacial density of 10^{10} cm^{-2}, a number typical for passivated Si wafers, there are only on average 30 traps on the surface of a 0.3 μm^2 grain, meaning that for a simple stochastic distribution of defects, one expects a distribution of actual number of defects for the same grain size. We have calculated the distribution of carrier lifetimes by using Equations 3 and 5 using lognormal distributions for both grain size and film thickness, and the results suggest that the variations of grain size and film thickness provide a good account for the observed variation in lifetimes (Figures S15,16 and Supplementary Note 3).

Physical Chemistry Chemical Physics Accepted Manuscript

Pursuant to the DOE Public Access Plan, this document represents the authors' peer-reviewed, accepted manuscript.
The published version of the article is available from the relevant publisher.

View Article Online
DOI: 10.1039/C6CP08770A

Published on 13 January 2017. Downloaded by National Renewable Energy Laboratory on 17/01/2017 08:41:44.

Similar to our current observations, there have been reports in the literature on variations in confocal luminescence intensity throughout perovskite thin films.[31] These variations were ascribed to variations in local trap density which causes the critical excitation density where the recombination turns over from being dominated by trapping to being dominated by bimolecular recombination to change. These studies were not able to resolve the individual grains and did not consider that carriers rapidly diffuse from the initial excitation spot throughout grains. Furthermore, it is clear from the current analysis that the rapid diffusion and the variation in grain size and film thickness cause the effective local light intensity to vary over orders of magnitude even if the excitation intensity does not change. This will cause the apparent turnover light intensity between trap-limited and bimolecular regimes to vary spatially simply because the grain size in the confocal spot varies spatially. Therefore, the variation in confocal PL intensity can simply be accounted for by variations in grain size and film thickness.

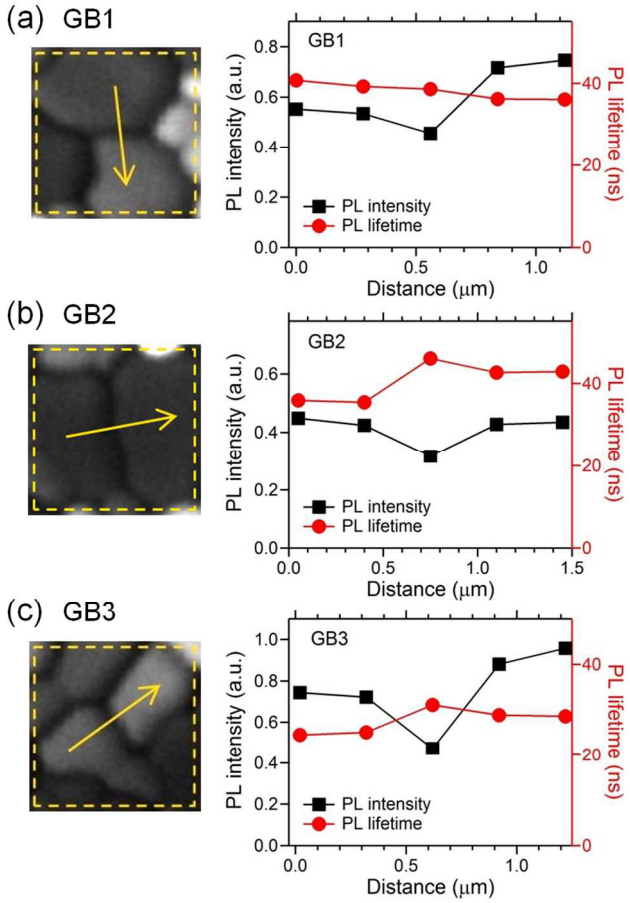

Figure 4. Typical line profiles across grain boundaries (GBs) between two neighboring grains with comparable PL intensity and lifetime. The three regions (GB1–3) are indicated as

Pursuant to the DOE Public Access Plan, this document represents the authors' peer-reviewed, accepted manuscript.
The published version of the article is available from the relevant publisher.

Physical Chemistry Chemical Physics Accepted Manuscript

View Article Online
DOI: 10.1039/C6CP08770A

Published on 13 January 2017. Downloaded by National Renewable Energy Laboratory on 17/01/2017 08:41:44.

yellow dashed squares in Figure 1a. Five consecutive regions (about 280-nm size) along each line scan were selected to get the TCSPC histograms. The intensity-weight PL lifetimes and total PL intensities from each region are shown as the red circles and black squares, respectively.

The modeling of luminescence lifetime as a function of grain area (discussed above) indicates that the GBs play a minor role in determining recombination kinetics in our $MAPbI_3$ perovskite thin films. This result is different from the general belief that, in comparison to the non-GB regions (GIs and GSs), GBs consist of more non-radiative recombination sites that should generally be reduced. To further examine the difference between GB and non-GB regions with respect to their luminescence property, we examined the luminescence lifetime and intensity distribution across two adjacent grains. These two neighboring grains were purposely selected to have similar FLIM lifetimes and intensities to facilitate the comparison. Figure 4 shows three typical line profiles and each line consists of five consecutive regions with the middle one centered at the GBs. Consistent with the FLIM image, all three GB regions exhibit lower (by 30%–50%) luminescence intensities than the non-GB areas, which agrees with a recent study by Ginger et al.[19] However, in contrast to this previous study, we find that the luminescence lifetimes of these GB regions are either similar to or slightly longer than those from the adjacent grain areas, suggesting that GBs are at least not significant NRR centers and, to some degree, can even suppress recombination. This is consistent with our modeling results, which cannot reproduce the FLIM results if there were significant NRR at GBs. Figure 5 shows a statistical analysis of the intensity and lifetime distributions for the entire FLIM image (Figure 1a). Figure 5a shows that the grain interiors have a median intensity of 421 counts per second per pixel (cps), while the grain boundaries have an intensity of 389 cps, a difference of 8%. At the same time, Figure 5b shows that the median lifetime increases from 30.9 to 32.7 ns going from the interior to the boundaries, a change of 6%.

Physical Chemistry Chemical Physics Accepted Manuscript

Pursuant to the DOE Public Access Plan, this document represents the authors' peer-reviewed, accepted manuscript.
The published version of the article is available from the relevant publisher.

View Article Online
DOI: 10.1039/C6CP08770A

Published on 13 January 2017. Downloaded by National Renewable Energy Laboratory on 17/01/2017 08:41:44.

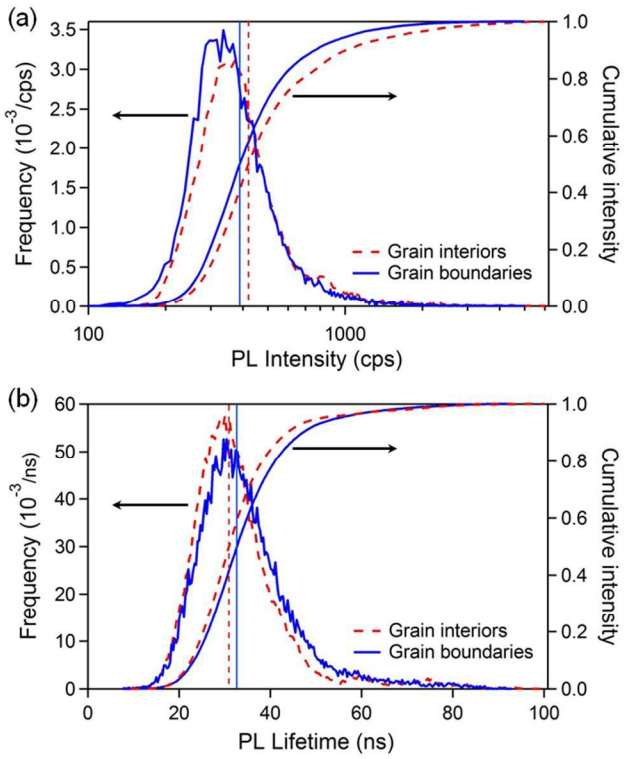

Figure 5. Statistical analysis of the (a) FLIM intensity and (b) FLIM lifetime over the entire image (Figure 1a) for the grain interiors (red dashed lines) and grain boundaries (blue continuous lines). The vertical lines show the median intensity and lifetimes. The grain boundaries have lower intensity but longer lifetime.

Conclusion

In summary, we have examined grain boundaries with respect to their interiors and surfaces in high-quality perovskite $MAPbI_3$ thin films using high-resolution confocal FLIM microscopy and theoretic modeling. The $MAPbI_3$ films were prepared by using a non-stoichiometric precursor to ensure that the grain size is suitable for these imaging studies. We have identified the importance of considering charge-carrier diffusion following the initial laser photoexcitation to properly understand the confocal PL imaging results. Analysis of the FLIM results, coupled with kinetic modeling of carrier decay processes, has led to several important observations about the roles of GBs and grain sizes on charge transport and recombination in our polycrystalline $MAPbI_3$ thin films. (1) Although GBs display lower luminescence intensities than their interiors/surfaces, the luminescence lifetimes at GBs are similar or slightly longer than lifetimes at the interiors/surfaces. This implies that GBs are not dominant non-radiative

Physical Chemistry Chemical Physics Accepted Manuscript

Pursuant to the DOE Public Access Plan, this document represents the authors' peer-reviewed, accepted manuscript.
The published version of the article is available from the relevant publisher.

View Article Online
DOI: 10.1039/C6CP08770A

Published on 13 January 2017. Downloaded by National Renewable Energy Laboratory on 17/01/2017 08:41:44.

recombination centers in comparison to the non-GB regions. (2) Grain boundaries are impervious to photocarriers explaining why each grain has approximately a single luminescence lifetime/intensity and why there are abrupt changes between neighboring grains. (3) The variations of confocal PL intensity are caused by changes in grain size, thickness, and possibly the stochastic distribution of traps.

Acknowledgements

The work at the National Renewable Energy Laboratory is supported by the U.S. Department of Energy under Contract No. DE-AC36-08GO28308. KZ and DK acknowledge the support from the U.S. Department of Energy SunShot Initiative under the Next Generation Photovoltaics 3 program (DE-FOA-0000990). YZ acknowledges the support on the FLIM instrumentation by the BioEnergy Science Center (BESC), a DOE Bioenergy Research Center funded by the Office of Biological and Environmental Research (BER) in the DOE Office of Science. JvdL acknowledges the support from the Division of Chemical Sciences, Geosciences, and Biosciences, Office of Basic Energy Sciences (DOE). MY and ZL acknowledge the support by the hybrid perovskite solar cell program of the National Center for Photovoltaics funded by the U.S. Department of Energy, Office of Energy Efficiency and Renewable Energy, Solar Energy Technologies Office.

References

1. A. Kojima, Teshima K., Shirai Y., Miyasaka T. Organometal halide perovskites as visible-light sensitizers for photovoltaic cells. *J. Am. Chem. Soc.* **131**, 6050-6051 (2009).
2. H.-S. Kim*, et al.* Lead iodide perovskite sensitized all-solid-state submicron thin film mesoscopic solar cell with efficiency exceeding 9%. *Scientific Reports* **2**, 591 (2012).
3. M. M. Lee, Teuscher J., Miyasaka T., Murakami T. N., Snaith H. J. Efficient hybrid solar cells based on meso-superstructured organometal halide perovskites. *Science* **338**, 643-647 (2012).
4. J. Burschka*, et al.* Sequential deposition as a route to high-performance perovskite-sensitized solar cells. *Nature* **499**, 316-319 (2013).
5. J. H. Heo*, et al.* Efficient inorganic-organic hybrid heterojunction solar cells containing perovskite compound and polymeric hole conductors. *Nat. Photonics* **7**, 487-492 (2013).

Physical Chemistry Chemical Physics Accepted Manuscript

Pursuant to the DOE Public Access Plan, this document represents the authors' peer-reviewed, accepted manuscript.
The published version of the article is available from the relevant publisher.

View Article Online
DOI: 10.1039/C6CP08770A

Published on 13 January 2017. Downloaded by National Renewable Energy Laboratory on 17/01/2017 08:41:44.

6. D. Y. Liu, Kelly T. L. Perovskite solar cells with a planar heterojunction structure prepared using room-temperature solution processing techniques. *Nat. Photonics* **8**, 133-138 (2014).
7. H. P. Zhou, *et al.* Interface engineering of highly efficient perovskite solar cells. *Science* **345**, 542-546 (2014).
8. D.-Y. Son, *et al.* Self-formed grain boundary healing layer for highly efficient ch3 nh3 pbi3 perovskite solar cells. *Nature Energy* **1**, 16081 (2016).
9. Q. Chen, *et al.* Under the spotlight: The organic-inorganic hybrid halide perovskite for optoelectronic applications. *Nano Today* **10**, 355-396 (2015).
10. Y. X. Zhao, Zhu K. Organic-inorganic hybrid lead halide perovskites for optoelectronic and electronic applications. *Chem. Soc. Rev.* **45**, 655-689 (2016).
11. N.-G. Park, Grätzel M., Miyasaka T., Zhu K., Emery K. Towards stable and commercially available perovskite solar cells. *Nature Energy* **1**, 16152 (2016).
12. Z. G. Xiao, Dong Q. F., Bi C., Shao Y. C., Yuan Y. B., Huang J. S. Solvent annealing of perovskite-induced crystal growth for photovoltaic-device efficiency enhancement. *Adv. Mater.* **26**, 6503-6509 (2014).
13. N. De Marco, *et al.* Guanidinium: A route to enhanced carrier lifetime and open-circuit voltage in hybrid perovskite solar cells. *Nano Lett.* **16**, 1009-1016 (2016).
14. B. Yang, *et al.* Perovskite solar cells with near 100% internal quantum efficiency based on large single crystalline grains and vertical bulk heterojunctions. *J. Am. Chem. Soc.* **137**, 9210-9213 (2015).
15. B. S. Tosun, Hillhouse H. W. Enhanced carrier lifetimes of pure iodide hybrid perovskite via vapor-equilibrated re-growth (verg). *J. Phys. Chem. Lett.* **6**, 2503-2508 (2015).
16. W. Zhang, *et al.* Enhanced optoelectronic quality of perovskite thin films with hypophosphorous acid for planar heterojunction solar cells. *Nat. Commun.* **6**, 10030 (2015).
17. M. J. Yang, Zhou Y. Y., Zeng Y. N., Jiang C. S., Padture N. P., Zhu K. Square-centimeter solution-processed planar ch3nh3pbi3 perovskite solar cells with efficiency exceeding 15%. *Adv. Mater.* **27**, 6363-6370 (2015).
18. K. Zhu, Miyasaka T., Kim J. Y., Mora-Sero I. Trend of perovskite solar cells: Dig deeper to build higher. *J. Phys. Chem. Lett.* **6**, 2315-2317 (2015).
19. D. W. deQuilettes, *et al.* Impact of microstructure on local carrier lifetime in perovskite solar cells. *Science* **348**, 683-686 (2015).
20. M. Vrucinic, *et al.* Local versus long-range diffusion effects of photoexcited states on radiative recombination in organic-inorganic lead halide perovskites. *Adv. Sci.* **2**, 136-136 (2015).
21. M. J. Simpson, Doughty B., Yang B., Xiao K., Ma Y.-Z. Imaging electronic trap states in perovskite thin films with combined fluorescence and femtosecond transient absorption microscopy. *J. Phys. Chem. Lett.* **7**, 1725-1731 (2016).
22. N. K. Noel, *et al.* Enhanced photoluminescence and solar cell performance via lewis base passivation of organic–inorganic lead halide perovskites. *ACS Nano* **8**, 9815-9821 (2014).
23. W. J. Yin, Shi T. T., Yan Y. F. Unique properties of halide perovskites as possible origins of the superior solar cell performance. *Adv. Mater.* **26**, 4653-4658 (2014).
24. R. Long, Liu J., Prezhdo O. V. Unravelling the effects of grain boundary and chemical doping on electron–hole recombination in ch3nh3pbi3 perovskite by time-domain atomistic simulation. *J. Am. Chem. Soc.*, DOI: 10.1021/jacs.1026b00645 (2016).

Physical Chemistry Chemical Physics Accepted Manuscript

Pursuant to the DOE Public Access Plan, this document represents the authors' peer-reviewed, accepted manuscript.
The published version of the article is available from the relevant publisher.

View Article Online
DOI: 10.1039/C6CP08770A

Published on 13 January 2017. Downloaded by National Renewable Energy Laboratory on 17/01/2017 08:41:44.

25. N. J. Jeon, Noh J. H., Kim Y. C., Yang W. S., Ryu S., Seok Il S. Solvent engineering for high-performance inorganic-organic hybrid perovskite solar cells. *Nat. Mater.* **13**, 897-903 (2014).
26. N. Ahn, Son D. Y., Jang I. H., Kang S. M., Choi M., Park N. G. Highly reproducible perovskite solar cells with average efficiency of 18.3% and best efficiency of 19.7% fabricated via lewis base adduct of lead(ii) iodide. *J. Am. Chem. Soc.* **137**, 8696-8699 (2015).
27. O. G. Reid, Yang M., Kopidakis N., Zhu K., Rumbles G. Grain-size-limited mobility in methylammonium lead iodide perovskite thin films. *ACS Energy Lett.* **1**, 561-565 (2016).
28. I. Visoly-Fisher, Cohen, Sr., Ruzin A., Cahen D. How polycrystalline devices can outperform single-crystal ones: Thin film cdte/cds solar cells. *Adv. Mater.* **16**, 879-883 (2004).
29. C.-S. Jiang, Noufi R., Ramanathan K., AbuShama J. A., Moutinho H. R., Al-Jassim M. M. Does the local built-in potential on grain boundaries of cu(in,ga)se2 thin films benefit photovoltaic performance of the device? *Appl. Phys. Lett.* **85**, 2625-2627 (2004).
30. D. Dziuba, Jurkiewicz P., Cebecauer M., Hof M., Hocek M. A rotational bodipy nucleotide: An environment-sensitive fluorescence-lifetime probe for DNA interactions and applications in live-cell microscopy. *Angew. Chem.-Int. Edit.* **55**, 174-178 (2016).
31. S. Draguta*, et al.* Spatially non-uniform trap state densities in solution-processed hybrid perovskite thin films. *J. Phys. Chem. Lett.* **7**, 715-721 (2016).
32. Y. Yang*, et al.* Observation of a hot-phonon bottleneck in lead-iodide perovskites. *Nat. Photonics* **10**, 53-59 (2016).
33. C. Wehrenfennig, Eperon G. E., Johnston M. B., Snaith H. J., Herz L. M. High charge carrier mobilities and lifetimes in organolead trihalide perovskites. *Adv. Mater.* **26**, 1584-1589 (2014).

Physical Chemistry Chemical Physics Accepted Manuscript

Pursuant to the DOE Public Access Plan, this document represents the authors' peer-reviewed, accepted manuscript.
The published version of the article is available from the relevant publisher.